RESEARCH ARTICLE | JUNE 09 2023

Electron bunch dynamics and emission in particle-in-cell simulations of relativistic laser–solid interactions: On density artifacts, collisions, and numerical dispersion ✓

Nicholas M. Fasano ; Matthew R. Edwards ; Julia M. Mikhailova ✉

Physics of Plasmas 30, 063904 (2023)
https://doi.org/10.1063/5.0140028

Physics of Plasmas ARTICLE pubs.aip.org/aip/pop

Electron bunch dynamics and emission in particle-in-cell simulations of relativistic laser–solid interactions: On density artifacts, collisions, and numerical dispersion

Cite as: Phys. Plasmas **30**, 063904 (2023); doi: 10.1063/5.0140028
Submitted: 26 December 2022 · Accepted: 25 May 2023 ·
Published Online: 9 June 2023

Nicholas M. Fasano,[1,a)] Matthew R. Edwards,[2] and Julia M. Mikhailova[1,b)]

AFFILIATIONS

[1]Department of Mechanical and Aerospace Engineering, Princeton University, Princeton, New Jersey 08544, USA
[2]Department of Mechanical Engineering, Stanford University, Stanford, California 94305, USA

[a)]Electronic mail: nfasano@princeton.edu
[b)]Author to whom correspondence should be addressed: j.mikhailova@princeton.edu

ABSTRACT

Sub-optical-cycle dynamics of dense electron bunches in relativistic-intensity laser–solid interactions lead to the emission of high-order harmonics and attosecond light pulses. The capacity of particle-in-cell simulations to accurately model these dynamics is essential for the prediction of emission properties because the attosecond pulse intensity depends on the electron density distribution at the time of emission and on the temporal distribution of individual electron Lorentz-factors in an emitting electron bunch. Here, we show that in one-dimensional collisionless simulations, the peak density of the emitting electron bunch increases with the increase in the spatial resolution of the simulation grid. When collisions are added to the model, the peak electron density becomes independent of the spatial resolution. Collisions are shown to increase the spread of the peaks of Lorentz-factors of emitting electrons in time, especially in the regimes far from optimum generation conditions, thus leading to lower intensities of attosecond pulses as compared to those obtained in collisionless simulations.

I. INTRODUCTION

At relativistic laser intensities, solid surfaces turn into fully ionized plasmas that reflect the incident light and emit high-order harmonics extending well into the x-ray range and forming attosecond pulses.[1–11] On a microscopic level, the process of relativistic high-order harmonic generation is well described by the coherent synchrotron emission (CSE) model that explains harmonic emission as a result of the sub-laser-cycle formation and acceleration of dense, nanometer-sized electron bunches.[12–16] The distribution of electrons in an emitting bunch plays a critical role in the efficiency as well as the temporal and spectral profiles of the emitted radiation whether the density distribution is viewed as a function of space at a fixed time[12,15,17,18] or as a function of the advanced time coordinate.[16,19] Previous work has shown that the electron bunches can be controlled by tailoring the driving laser's waveform to achieve enhanced harmonic efficiency.[20–24] Manipulating the electron bunches to control the properties of the harmonic radiation requires a detailed understanding of how the electron bunch evolution depends on the laser and plasma parameters.

The particle-in-cell (PIC) method, extensively used to numerically simulate laser–plasma interactions,[25–28] employs physical approximations and introduces numerical artifacts. To solve Maxwell's equations on a grid, conventional PIC codes utilize a finite-difference time-domain (FDTD) method, the Yee solver,[29] which is subject to numerical dispersion.[30–38] Numerical dispersion poses a significant challenge for modeling high-order harmonics that comprise a broad range of frequencies. Recently, pseudo-spectral Maxwell solvers based on fast Fourier transforms have been implemented to mitigate numerical dispersion and noise,[39–44] and dispersion-free propagation of harmonics has been demonstrated.[41] The PIC method also employs finite-sized macroparticles which represent a number of real particles in the system. Macroparticles accurately model long-range, collective plasma phenomena, but reduce the magnitude of the electromagnetic fields for short-range, collisional interactions.[45] To restore these short-range interactions, Monte Carlo-based algorithms for modeling binary collisions between macroparticles were developed,[46–52] and have been applied to short-pulse laser–solid interaction studies.[53–55] The binary collision model works by randomly pairing two particles within the same cell of the computational grid and then stochastically scatters the particles based on the Coulomb cross section. Monte Carlo collision models were originally proposed for non-relativistic interactions and between macroparticles with equal weighting[46] but have advanced in recent years to accurately handle collisions between relativistic particles[49,50,56] and macroparticles with arbitrary weight.[48,51]

Here, we aim to examine the characteristic features in the spatial distributions of electron densities at times before and near the time of attosecond pulse emission and understand the effect of spatial resolution, collisions, and numerical dispersion in conventional PIC simulations on the properties of accelerated electron bunches and their emission. Using the EPOCH PIC code,[28] we provide a detailed analysis of the electron bunch evolution for different relativistic laser–solid interaction scenarios in collisionless and collisional simulations. We demonstrate the appearance of unphysical density spikes with the peak density growing with increasing spatial resolution in collisionless simulations. We show, however, that these density spikes have no effect on the intensity of emitted harmonic radiation. We then analyze the effects of collisions on the electron bunches, showing that the unphysical density spikes disappear with collisions and, in addition, collisions are shown to increase the spread in time of the peak Lorentz factors of emitting electrons within the electron bunch, which reduces attosecond pulse intensity compared to collisionless simulations.

II. ATTOSECOND ELECTRON BUNCH DYNAMICS

Since the formation of individual electron bunches in relativistic laser–solid interactions occurs on a sub-laser-cycle timescale, we consider single-cycle laser pulses interacting with semi-infinite plasma slabs, which result in the continuous spectra of plasma emission analyzed below. We model normal and oblique incidence interactions in a one-dimensional geometry, where a relativistic transform to a boosted reference frame is used for oblique incidence.[57,58] The incident laser's wave vector is at an angle θ with respect to the x-axis in the x–y plane, where the target's normal vector points in the negative x direction. The laser pulse strength is given by the relativistic amplitude $a_0 = eE_L/(m\omega_L c)$, where c is the speed of light, e and m are the electron's charge and mass, E_L is the maximum of the electric field envelope, and ω_L is the driving laser's angular frequency. For all simulations, the laser was p-polarized with a central wavelength of $\lambda_L = 800$ nm and had a Gaussian temporal profile with a full-width-half-maximum of 2.7 fs. The plasma slab has a step-like density profile with an initial electron number density of N_0, where N_0 is normalized by the critical density $[n_c = m\omega_L^2/(4\pi e^2)]$. We treat ions as an immobile background, which is a reasonable assumption for single-cycle interactions. The simulations use a second-order FDTD scheme to solve Maxwell's equations, for which the time step, Δt, is determined by the Courant–Friedrichs–Lewy (CFL) number, $C = c\Delta t/\Delta x$, where Δx is the size of the spatial cell of the numerical grid. The simulations presented here use a spatial resolution between 100 and 100 000 cells per laser wavelength, a CFL number between 0.50 and 1.0, and between 25 and 150 particles/cell, where all particles are represented by a first-order b-spline (triangle) shape function unless otherwise stated.

In this work, we are interested in the evolution of the electron number density (N_e, which is normalized by n_c), the distribution of electron relativistic Lorentz factors (γ) as a function of the advanced time coordinate ($t_a = t + |x_o - x|/c$, where x_o is the observer position and x is the position of the electron), and the attosecond pulse generation efficiency. The reflected radiation is analyzed by first recording the reflected electric field in time at a fixed spatial location of $3\lambda_L$ from the initial vacuum–plasma interface for a duration of at least four laser periods before and after the arrival of the center of the reflected laser field's temporal envelope. The spectral intensity, $I(\omega)$, is then computed as the Fourier transform of the reflected field over this time window. Finally, the electric fields of attosecond pulses, E_a, are obtained by filtering the spectra in the frequency range $\omega_{LF} < \omega/\omega_L < \omega_{UF}$ and inverse Fourier transforming back to the time domain. The attosecond pulse generation efficiency, η_{atto}, is defined as the peak value of E_a^2/E_L^2. The spectral efficiency of frequency upconversion, η_{spec}, is calculated by integrating $I(\omega)$ in the frequency range $\omega_{LF} < \omega/\omega_L < \omega_{UF}$ and then dividing by the integrated spectral intensity of the incident laser. The incident and reflected spectra have been normalized by the peak value of the incident laser's spectral intensity.

The attosecond pulse emission and the sub-cycle plasma dynamics in relativistic laser–solid interactions are shown in Fig. 1. In the time domain [Fig. 1(a)], the reflected waveform is substantially distorted compared to the incident one, indicating the presence of high-frequency radiation. Transforming to the frequency domain [Fig. 1(b)], we observe a broadband, continuous spectrum which follows a power-law scaling up to a frequency cutoff ($\omega/\omega_L \approx 200$) after which a steeper decline in spectral intensity is observed. The dashed orange line in Fig. 1(b) represents a power-law fit $[I(\omega) \propto (\omega/\omega_L)^{-p}]$ in the frequency range $1 < \omega/\omega_L < 10$ but is seen to provide a good fit up until the frequency cutoff. Filtering out the low harmonic orders ($\omega/\omega_L < 30$) and transforming back to the time domain results in an attosecond pulse, as shown by the red line in Fig. 1(a).

The spatial distributions of the electron density for particular instants of time during the interaction are presented in Figs. 1(c) and 1(d). The time $t/T_L = 0$ corresponds to the instant when the laser's electric field node (the node that precedes the attosecond pulse emission) first meets the plasma surface, where the electric field nodes are defined as the points in space where the incident electric field is zero. As the laser starts interacting with the plasma, the $v \times B$ force and the force from the component of the laser's transverse electric field that acts in the target's normal direction combine to displace the electrons from their initial location, forming a dense electron nanobunch [Fig. 1(c)]. The displacement of the electron surface results in a built-up electrostatic restoring force which subsequently accelerates the electron bunch toward the specular direction where it narrows in space and increases in peak density, emitting an attosecond pulse at $t/T_L = 0.63$ [Fig. 1(d)]. The dynamics of a single emitting electron within the bunch are shown in Fig. 1(e), where the particle data are plotted in the reference frame (x_1, y_1), which is rotated by an angle θ with respect to (x, y), so that x_1 is parallel to the direction of specular reflection. The time of emission corresponds to the spike in the relativistic Lorentz factor, γ_{x1}, when the electron's velocity is along the specular direction and the acceleration is perpendicular to the velocity, which is in agreement with the CSE model.[14]

The efficiency of attosecond pulse generation is highest when the laser force, which is a function of a_0, and the plasma restoring force, which is a function of N_0, are of similar magnitude, and not necessarily at exactly the same time.[16,23] This balance can be characterized by the similarity parameter $S = N_0/a_0$, or $1/S = a_0/N_0$, which arises from the similarity analysis of laser–plasma interactions in the ultra-relativistic

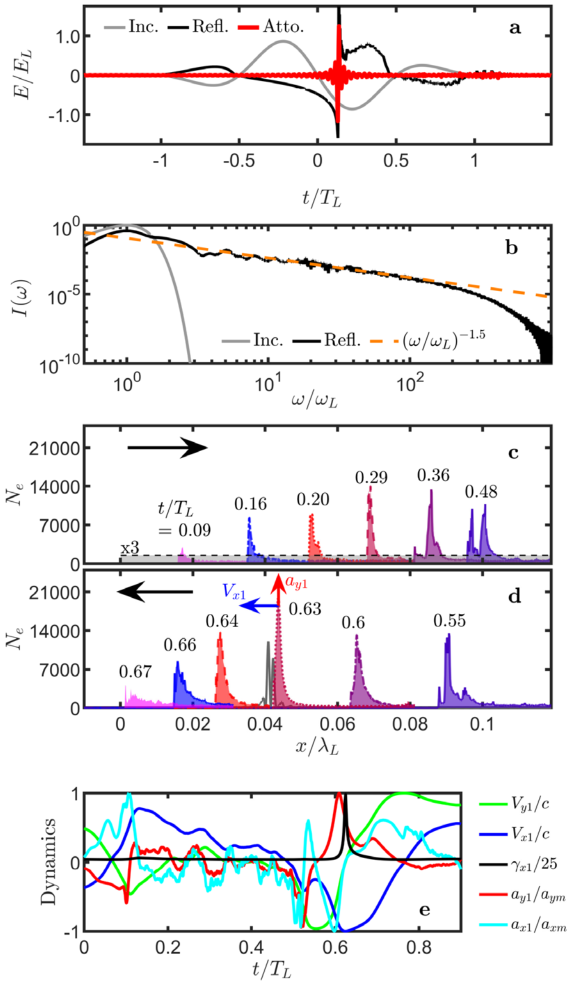

FIG. 1. Attosecond pulse emission [(a) and (b)] and sub-cycle density dynamics [(c) and (d)] of relativistic electron bunches near the surface of a plasma mirror from PIC simulations. Simulation parameters are $\theta = 30°$, $a_0 = 175$, $N_0 = 500$, $\lambda_L/\Delta x = 8000$, particles/cell = 50, and $C = 0.95$. (a) The electric fields of incident (gray), reflected (black), and filtered attosecond pulse (red) as a function of time. (b) Spectral intensity of the incident (gray) and reflected (black) laser pulse, and a power-law fit of the reflected spectrum in the frequency range $1 < \omega/\omega_L < 10$ (dashed). [(c) and (d)] Spatial distribution of the electron density (N_e) for different times within a single cycle of the incident laser field. (c) Electron bunch is moving to the right into the bulk of the plasma pushed by the laser field. (d) Electron bunch is moving to the left toward vacuum. The attosecond pulse is emitted at $t/T_L = 0.63$ when the velocity and acceleration are perpendicular to each other. (e) Dynamics of a selected electron leading up the emission of the attosecond pulse. The dynamics are plotted in a coordinate system (x_1, y_1) that is parallel and perpendicular to the specular direction. The two components of acceleration have been normalized to their maximum values.

limit.[59] The brightest attosecond pulses occur when $a_0/N_0 \approx 0.3$ for normal incidence interactions and for $a_0/N_0 \approx 0.5$ for oblique incidence interactions.[16] In Fig. 2, we show the evolution of the electron density spatial distribution and the emitted attosecond pulses for normal ($\theta = 0°$) and oblique ($\theta = 30°$) incidences and various ratios of a_0/N_0. In each subplot, the electron bunch evolves from the time when the electron bunch has its maximum displacement from the initial plasma–vacuum interface (T_{MaxDisp}) through the time when the attosecond pulse is emitted (T_{Emission}), which is calculated by back-propagating the emitted attosecond pulse until the time instant when the peak of the attosecond pulse and the leading edge of the electron bunch is located at the same point in space. The dashed line indicates the peak density of the electron bunch at different points in time.

For $a_0/N_0 \lesssim 0.1$ [Figs. 2(a) and 2(b)], the electron bunch evolution in normal and oblique incidence simulations is similar: the peak density of the electron bunch slowly drops, while its width remains roughly the same. The attosecond pulse is emitted at $t/T_L \approx 0.5$, at which point the electron bunch has expanded close to the original density, resulting in inefficient attosecond pulse generation. In contrast, for $a_0/N_0 \gtrsim 0.2$ [Figs. 2(d)–2(k)], the electron bunch is compressed in space as it accelerates toward vacuum for both the normal and obliquely incident cases. For normal incidence interactions, the electron bunch never reaches a peak density higher than what is obtained at T_{MaxDisp} but better maintains the peak density through T_{Emission}, where the peak density is seen to decrease by only 30% from T_{MaxDisp} to T_{Emission} for $a_0/N_0 = 0.55$ and not at all for $a_0/N_0 = 0.35$. For oblique incidence interactions, emission occurs when the electron bunch has a peak density higher than that obtained at T_{MaxDisp} [Figs. 2(h) and 2(k)]. This results in more efficient attosecond pulse generation than that obtained for values of $a_0/N_0 \lesssim 0.1$. Note that the times of the attosecond pulse emission extend beyond one-half of a laser period in the interactions with $a_0/N_0 \gtrsim 0.2$ as a result of the increased displacement of the electron bunches from the initial plasma–vacuum interface.

III. RESOLUTION-DEPENDENT SPIKES OF THE ELECTRON DENSITY

As the intensity, spectra, and duration of the emitted radiation critically depend on the electron density distribution at the time of emission and the temporal distribution of individual electron Lorentz-factors in an emitting electron bunch, the capacity of PIC simulations to accurately model electron density dynamics is essential for the prediction of the emission properties. This brings up questions regarding the effects of the spatial resolution and number of particles/cell present at the start of the simulation on the electron density dynamics. To address these questions, we first examine the dependence of the peak density of electron bunches on the spatial cell size of the numerical grid. The peak electron density (N_{peak}) at the times T_{MaxDisp} and T_{Emission} is potted as a function of $\lambda_L/\Delta x$ in Fig. 3(i) for different sets of simulation parameters: (a) $\theta = 0°$, $a_0 = 40$, $N_0 = 200$; (b) $\theta = 30°$, $a_0 = 175$, $N_0 = 500$; (c) $\theta = 30°$, $a_0 = 325$, $N_0 = 500$. As is shown in Fig. 3(i), the peak electron density exhibits a power-law growth as a function of $\lambda_L/\Delta x$ and does not converge to a fixed value even at an extremely high resolution of $\lambda_L/\Delta x > 35\,000$.

The spatial distributions of the electron density at the times T_{MaxDisp} and T_{Emission} are plotted in Figs. 3(ii) and 3(iii), respectively. For each instant of time, the distributions are plotted with a dotted blue line for simulations with $\lambda_L/\Delta x = 4000$ and a solid cyan line for simulations with $\lambda_L/\Delta x = 35\,000$. In these collisionless PIC simulations, we observe the presence of narrow density spikes contained within a single cell of the numerical grid. The number of density spikes, as well as the peak density of those spikes, increases with higher spatial resolution. At the highest resolutions considered here, a large

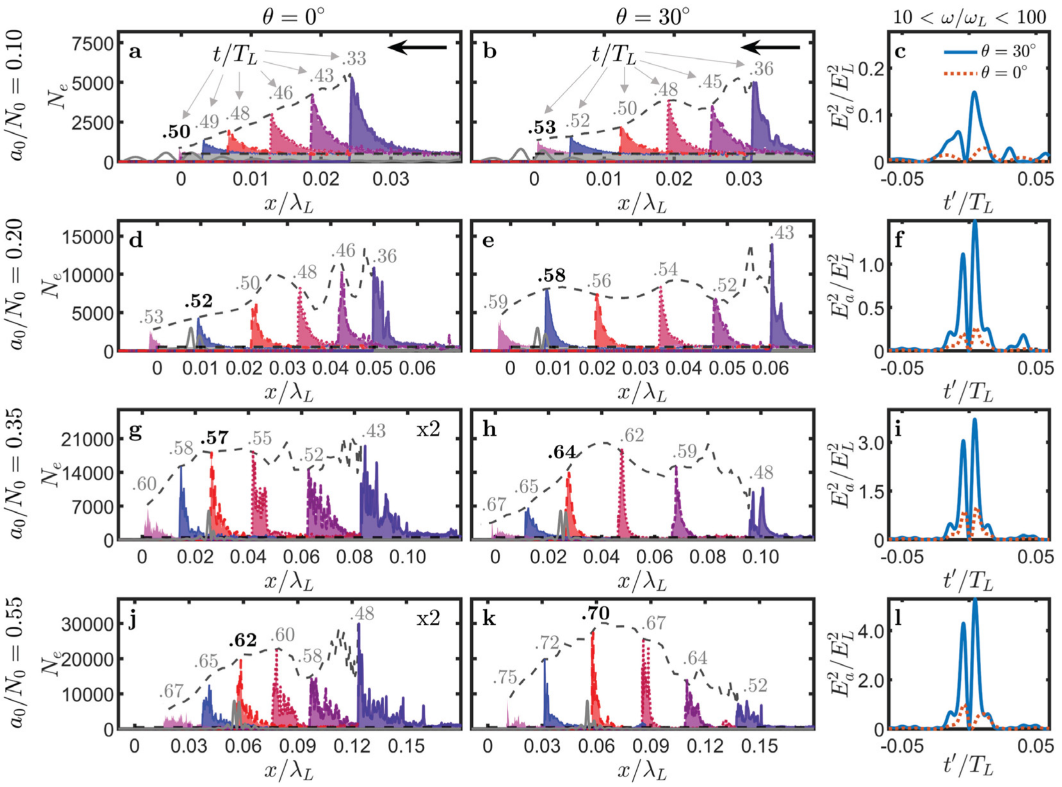

FIG. 2. Spatial distributions of the electron number density (N_e) illustrating the electron bunch evolution from the time when the electron bunch has its maximum displacement from the initial plasma–vacuum interface (T_{MaxDisp}) through the time when the attosecond pulse is emitted (T_{Emission}). The simulation parameters are $N_0 = 500$, particles/cell = 50, $\lambda_L/\Delta x = 8000$, $C = 0.95$, and $a_0/N_0 = 0.10$ [(a)–(c)], $a_0/N_0 = 0.20$ [(d)–(f)], $a_0/N_0 = 0.35$ [(g)–(i)], and $a_0/N_0 = 0.55$ [(j)—(l)]. The dashed gray line marks the electron bunch's peak density as it evolves from right to left and emits the attosecond pulse. The bold times within each subplot indicate the time of emission. The density distributions in subplots (g) and (j) have been scaled by a factor of two, as indicated in the upper right corner, so that the distribution of the electron density is easier to visualize at this scale. For each case of a_0/N_0, the right panels plot the attosecond pulses as a function of time from the normal and oblique incidence interaction, where we have artificially overlaid the two attosecond pulses and centered them at a time of zero so that their profiles and peaks can be easily compared. The attosecond pulses were constructed using radiation in the frequency range $10 < \omega/\omega_L < 100$.

number of electrons ($N_0 > 20\,000$) is compressed into a single cell of a width $\Delta x \approx 0.08$ Å. The peak density in the spikes is about an order of magnitude higher than the average density in the bunch. The appearance of these single-cell density spikes and the corresponding growth of the peak electron density result from the fact that closely spaced particles tend to accumulate in a single cell of the numerical grid.

To eliminate this unphysical effect, we consider collisional PIC model using the Monte Carlo-based binary collision algorithm[47,48,50] incorporated in the EPOCH code. We include electron–ion and electron–electron collision processes in all simulations. The results of collisional simulations are shown by red circles and squares in Fig. 3(i). With collisions, the peak density of the electron bunch initially follows the same power-law growth as a function of $\lambda_L/\Delta x$ as in the simulations without collisions, but eventually, it converges to a fixed value at a spatial resolution which depends on the laser and plasma parameters but is less than 10 000 cells per fundamental wavelength in all cases. Additionally, in contrast to collisionless simulations where the increased spatial resolution leads to the appearance of multiple density spikes confined within single cells, collisional model yields smoother density distributions [solid black line in Figs. 3(ii) and 3(iii)] without the single-cell density spikes even at a high spatial resolution of $\lambda_L/\Delta x = 35\,000$.

The unphysical growth in the peak density of the electron bunch present in collisionless simulations does not change with the number of particles/cell present at the start of the simulation or on the shape function used to represent the particles. In Fig. 4(a), the peak density of the electron bunch is plotted as a function $\lambda_L/\Delta x$ for simulations with collisions and particles/cell = 50 (red triangles) and simulations without collisions and particles/cell = 25 (green circles), 50 (blue squares), and 100 (black triangles). All other parameters are the same as those used for the simulations presented in Fig. 3(a). Here, we see that at T_{MaxDisp} and T_{Emission} the peak density of the electron bunch follows the same power-law growth independent of the number of particles/cell. Similarly, increasing the order of the particle shape function does not remove the resolution-dependent density spikes since the spikes arise from the clumping of electrons within a cell of the numerical grid rather than from sampling noise. This is illustrated in Fig. 4(b) where the peak density of the electron bunch is plotted as a function $\lambda_L/\Delta x$ for simulations with collisions and a first-order b-spline (triangle) shape function (red triangles) and simulations without

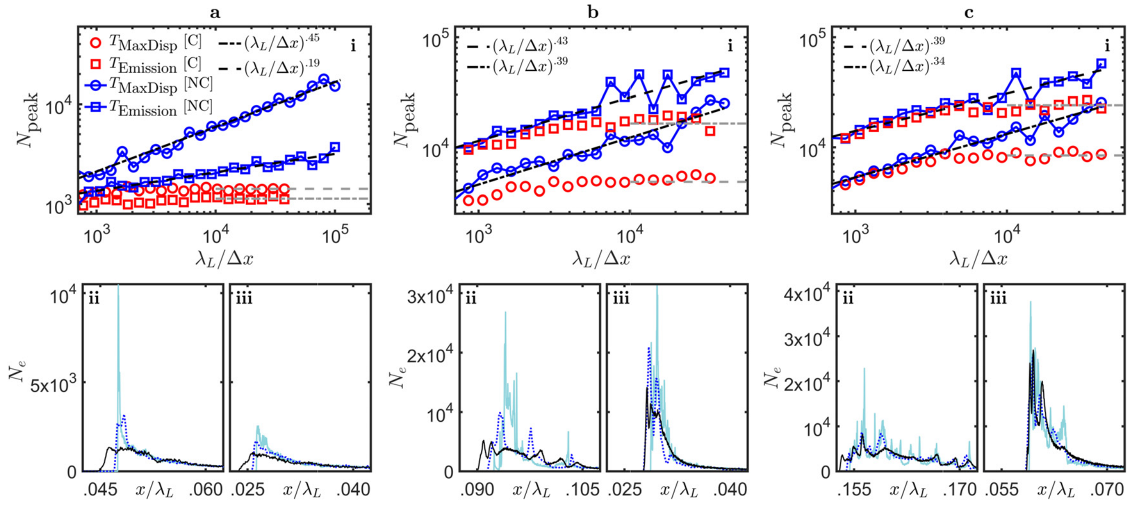

FIG. 3. Effects of spatial resolution on the density distribution of the electron bunch modeled with and without collisions for (a) $\theta = 0°$, $a_0 = 40$, $N_0 = 200$; (b) $\theta = 30°$, $a_0 = 175$, $N_0 = 500$; and (c) $\theta = 30°$, $a_0 = 325$, $N_0 = 500$. For all simulations, $C = 0.95$ and particles/cell = 50. (i) The peak density, $N_{\rm peak}$, in collisionless [NC] (blue circles and squares) and collisional [C] (red circles and squares) simulations as a function of $\lambda_L/\Delta x$. For the collisionless cases, the black dashed lines show power-law fits to the peak density. For the collisional cases, a horizontal gray dashed line is plotted at the average value of $N_{\rm peak}$ for $\lambda_L/\Delta x > 10\,000$. (ii) The electron density spatial distribution near the time when the electron bunch has its maximum displacement from the plasma–vacuum interface ($T_{\rm MaxDisp}$). Distributions from collisionless simulations are plotted in dark blue for $\lambda_L/\Delta x = 4000$ and cyan for $\lambda_L/\Delta x = 35\,000$. Distributions from collisional simulations are plotted in black at $\lambda_L/\Delta x = 35\,000$. (iii) Same as (ii) but the distribution is plotted at the time when the attosecond pulse is emitted ($T_{\rm Emission}$).

collisions [NC] and a zeroth-order b-spline (top-hat) shape function (green circles), a first-order b-spline (triangle) shape function (blue squares), and a third-order b-spline shape function (black triangles).

The single-cell density spikes in collisionless simulations do not affect the convergence of the radiated fields as verified in Figs. 5(a)–5(c), where we see the reflected spectra, temporal intensity profiles, and attosecond pulse efficiency converge with increasing spatial resolution. The emitted attosecond pulses are able to converge despite the lack of convergence of the electron bunch peak density since these density spikes arise from a grouping of electrons within the cell of the numerical grid, which is much smaller than the shortest wavelength of interest. Since the number of electrons within the density spike remains fixed and only the cell size changes when the spatial resolution is increased, the radiated fields of the electrons converge with increasing spatial resolution. Note that the differences between the pulse profiles in Fig. 5(b) at low spatial resolutions are due to the fact that the harmonics are under-resolved and numerical dispersion has an effect on the pulse shape. A detailed discussion of the effects of the spatial and temporal resolution on the emitted attosecond pulses is presented in the Appendix.

IV. EFFECTS OF COLLISIONS ON ELECTRON BUNCH DYNAMICS AND ATTOSECOND PULSE INTENSITY

In Sec. III, we showed that collisionless simulations allow for resolution-dependent spikes in the electron bunch, but that the attosecond pulses due converge with increasing resolution. Additionally, we showed that in collisional simulations, there are no unphysical density spikes and the electron bunch is smoother compared to collisionless simulations. In this section, we address the final question of how do the radiated attosecond pulses and spectra differ between collisional and collisionless simulations. In Fig. 6, the attosecond pulse generation efficiency with and without collisions is plotted as a function of a_0/N_0 for three different initial plasma densities. There are two regimes where simulations with and without collisions have the same attosecond pulse efficiency. The first is in the limit where $a_0/N_0 \approx 1$ for a fixed N_0 and the second is when $N_0 > 500$ for a fixed a_0/N_0. Both of these limits require $a_0 > 100$, which is a higher laser field strength than that currently achievable in ongoing experiments. For parameter regimes away from these two limits, collisions lower the attosecond pulse efficiency, where the greatest reduction occurs for a_0/N_0 greater than 0.2, but less than 0.6. The reduction in attosecond pulse efficiency reaches up to a factor of 5 in the chosen frequency range of $80 < \omega/\omega_L < 300$. We have found that the amount of reduction is dependent on the chosen frequency range and would be completely negligible if the frequency range of $10 < \omega/\omega_L < 100$ was used. To understand how the entire spectra are affected by collisions, we return to modeling the electron bunch dynamics prior to attosecond pulse emission.

In Fig. 7, the spatial distribution of the electron density at particular times before the emission of the attosecond pulse is plotted for simulations with and without collisions at four different values of a_0/N_0. For $a_0/N_0 < 0.35$, collisions have the effect of lowering the peak density of the electron bunch, especially near the time when the electron bunch is at its maximum displacement from the initial plasma–vacuum interface. As a_0/N_0 is increased to values $\gtrsim 0.35$, the electron density spatial distributions become identical at all instants of time, apart from the single-cell density spikes present in collisionless simulations for which we have already shown have negligible effect on the emitted attosecond pulses. Also shown in Fig. 7 are the spectra and attosecond pulses of the reflected electric field. For all values of a_0/N_0, the simulations with and without collisions produce identical harmonic intensity for low frequencies. However, for $a_0/N_0 \lesssim 0.50$, the spectra produced from simulations with collisions have a lower

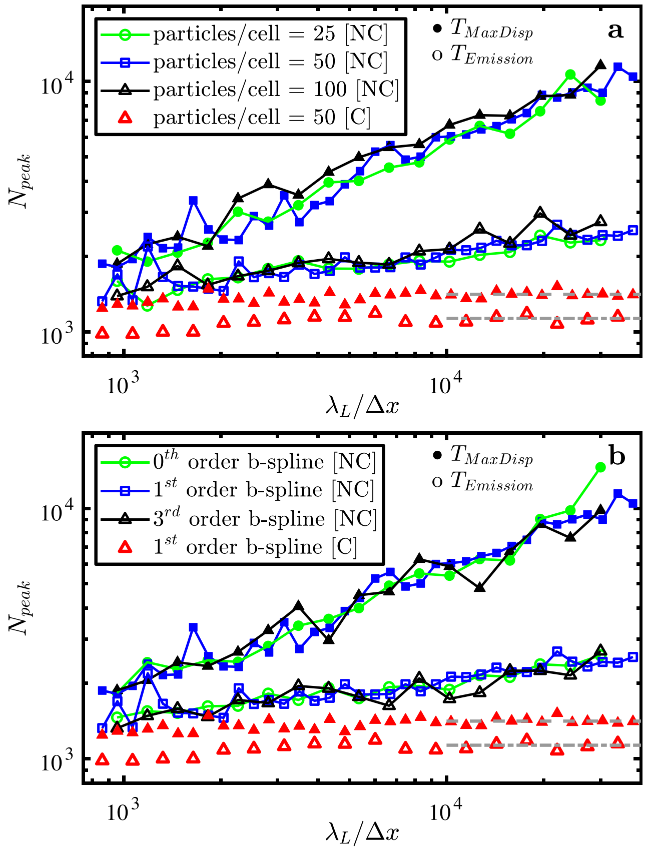

FIG. 4. (a) Peak density of the emitting electron bunch (N_{peak}) as a function of spatial resolution for simulations with collisions [C] and particles/cell = 50 (red triangles) and for simulations without collisions [NC] and particles/cell = 25 (green circles), 50 (blue squares), and 100 (black triangles). (b) N_{peak} as a function of spatial resolution for simulations with collisions [C] and a first-order b-spline (triangle) shape function (red triangles) and for simulations without collisions [NC] and a zeroth-order b-spline (top-hat) shape function (green circles), a first-order b-spline (triangle) shape function (blue squares), and a third-order b-spline shape function (black triangles). For both plots, the shaded symbols denote the peak density at T_{MaxDisp} and open symbols denote the peak density at T_{Emission}. Unless otherwise indicated, all simulations use $\theta = 0°$, $a_0 = 40$, $N_0 = 200$, $C = 0.95$, particles/cell = 50, and the particles are represented by a first-order b-spline. For the collisional cases, a horizontal gray dashed line is plotted at the average value of N_{peak} for $\lambda_L/\Delta x > 10\,000$.

frequency cutoff compared to collisionless simulations. Therefore, the intensity of attosecond pulses produced from simulations with collisions will be reduced only if a frequency range after the frequency cutoff is used, which for the spectra of Fig. 7 occurs at $\omega/\omega_L \approx 90$.

Within the framework of the CSE model, the location of the frequency cutoff can be determined by analyzing the distribution of the relativistic Lorentz factors of the emitting electrons within the electron bunch.[16,19] Analytically, the reflected spectral intensity can be calculated with the following equation:[12]

$$I(\omega) \propto |\tilde{f}(\omega)|^2 \omega^{-4/3} \left\{ \mathrm{Ai}' \left[(\omega/\omega_\gamma)^{2/3} \right] \right\}^2. \tag{1}$$

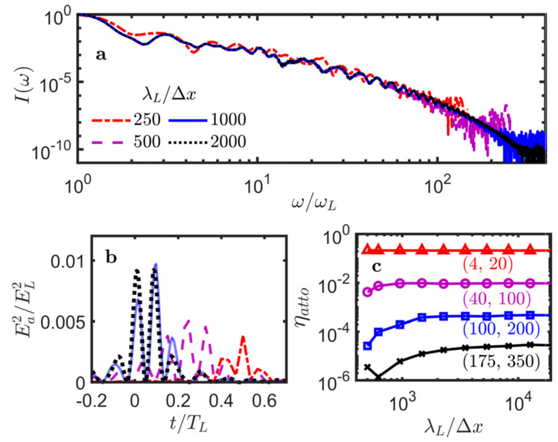

FIG. 5. Effects of the spatial resolution on the (a) reflected spectra, (b) the attosecond pulse temporal profile, and (c) the attosecond pulse efficiency in collisionless simulations for the parameters $\theta = 0°$, $a_0 = 20$, $N_0 = 100$, particles/cell = 100, and $C = 0.95$. In (b), the attosecond pulses were constructed using radiation in the frequency range $40 < \omega/\omega_L < 100$. In (c), the attosecond pulse efficiency was computed using radiation in the frequency range $(\omega_{LF}, \omega_{UF})$, where $\omega_{LF} < \omega/\omega_L < \omega_{UF}$.

In Eq. (1), $\omega_\gamma = \sqrt{8\alpha}\gamma^3$, where α is a constant calculated from the electron trajectories, $\gamma = 1/\sqrt{1 - v^2/c^2}$ is the Lorentz factor of the electrons at the time of emission, Ai$'$ is the derivative of the Airy function of the first kind, and $\tilde{f}(\omega)$ is the Fourier transform of the electron bunch shape function. It has been shown, across a wide range of laser and plasma parameters, that the shape of the electron bunch can be approximated as a step function since the peak Lorentz factors of the electrons abruptly jump to their maximum value at the leading edge of the distribution.[16] As a consequence, when the emitted wavelengths have a comparable size to the emitting electron bunch width, a

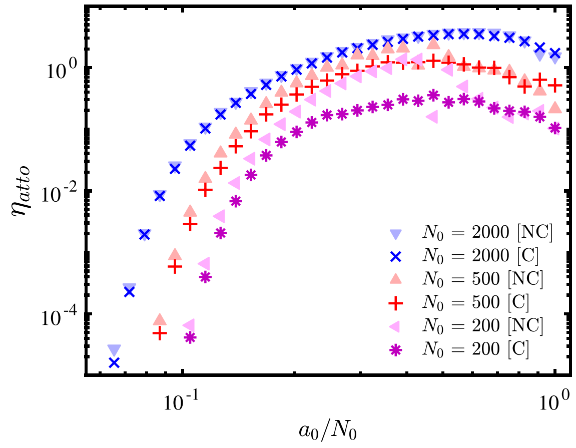

FIG. 6. Attosecond pulse generation efficiency, η_{atto}, as a function of a_0/N_0 for three different values of N_0, where the attosecond pulses were constructed using radiation in the frequency range $80 < \omega/\omega_L < 300$. Shaded triangles indicate simulations without collisions [NC]. The other symbols indicate simulations with collisions [C]. For all simulations $\theta = 30°$, $\lambda_L/\Delta x = 4000$, particles/cell = 100, and $C = 0.95$.

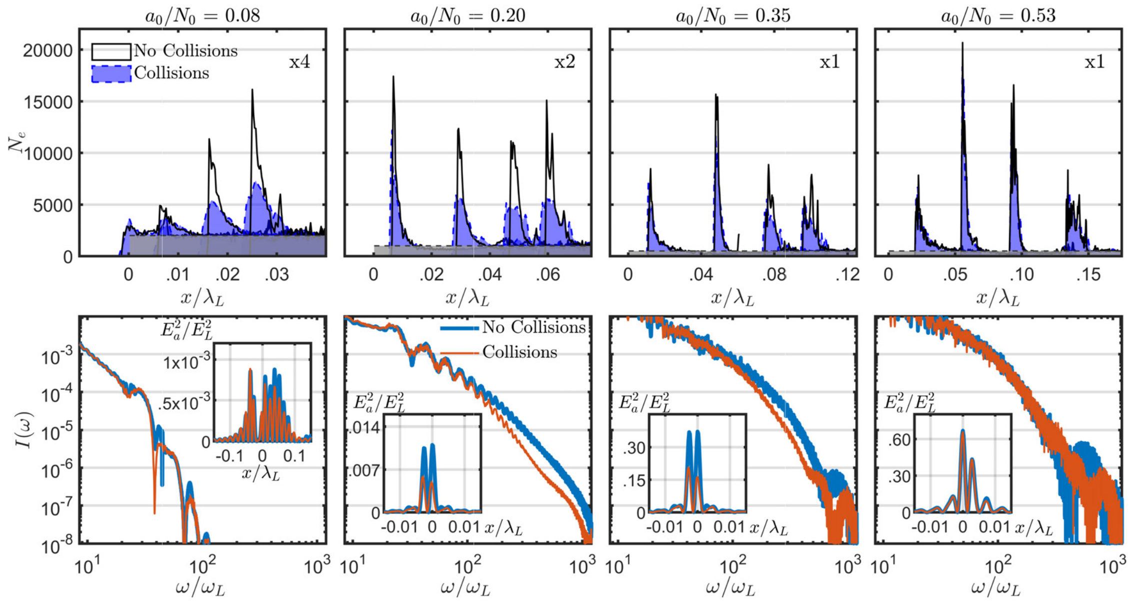

FIG. 7. Comparison of the electron density spatial distribution, the reflected spectral intensity, and the emitted attosecond pulse for simulations with and without collisions for the parameters $\theta = 30°$, $N_0 = 500$, $\lambda_L/\Delta x = 8000$, particles/cell = 150, $C = 0.95$, and varied a_0. The top row shows the evolution of the electron bunches from T_{MaxDisp} through T_{Emission} for simulations without collisions (solid black lines without shading) and for simulations with collisions (dashed blue lines with shading). The distributions in the left two plots have been scaled up by the factor listed in the upper right corner of the plot to allow for comparison of the profiles across all four values of a_0/N_0. The bottom row plots the reflected spectral intensity for both the collisional and collisionless cases. The inset plots on the bottom row compare the attosecond pulses which were constructed using radiation in the frequency range $100 < \omega/\omega_L < 300$ since that is where we observe the greatest discrepancy between collisional and collisionless simulations. For $a_0/N_0 = 0.08$, a frequency interval of $30 < \omega/\omega_L < 100$ was used because this interaction is less efficient, and for $\omega/\omega_L > 100$, the intensity drops below the noise level of the simulation.

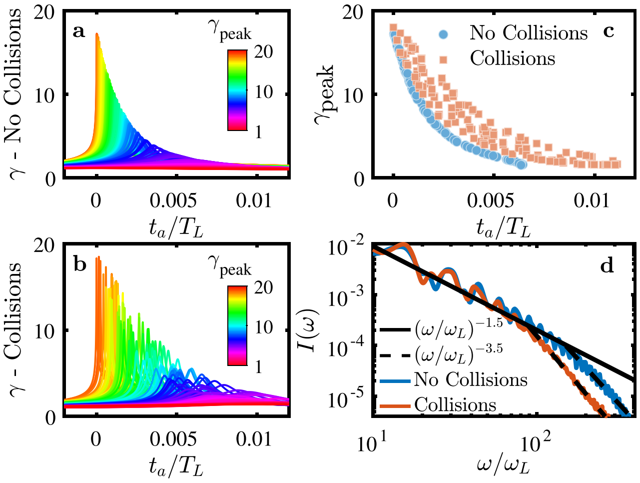

FIG. 8. Comparison of the distribution of Lorentz factors for emitting electrons within the electron bunch for simulations with and without collisions (a) distribution of the relativistic Lorentz factors of emitting electrons as a function of the advanced time coordinate for a collisionless simulation. The Lorentz factors are colored according to their peak value, γ_{peak}, as indicated by the colorbars. (b) Same as (a) but with collisions simulated. (c) Shows only the peak value of the Lorentz factors from (a) and (b) illustrating the spread of the emitting electron bunch when collisions are simulated. (d) Reflected spectra of the two cases showing the earlier bunch width-induced frequency cutoff when collisions are simulated. The simulation parameters are $\theta = 45°$, $a_0 = 80$, $N_0 = 200$, $\lambda_L/\Delta x = 10\,000$, particles/cell = 100, and $C = 0.95$.

transition of spectral scaling from the original ω^{-p} power-law to ω^{-p-2} takes place as a result of destructive interference between radiation emitted from different electrons within the electron bunch.

In Fig. 8, the distribution of Lorentz factors for individually emitting electrons within the electron bunch is plotted as a function of the advanced time coordinate for a collisionless [Fig. 8(a)] and collisional [Fig. 8(b)] simulation. Here, we see that, although the electrons within the emitting electron bunch have similar peak Lorentz factors in both cases, the overall spread in time of the peak Lorentz factors is greater when collisions are modeled [Fig. 8(c)]. This increased spread in the peak of the Lorentz factors results in an earlier frequency cutoff for the case with collisions as illustrated in Fig. 8(d). If we define the bunch width-induced frequency cutoff (ω_b) to be the frequency at which the spectral intensity drops by a factor of $1/e$ below its initial power-law scaling, then, $\omega_b/\omega_L \approx 250$ in the collisionless simulation and $\omega_b/\omega_L \approx 150$ in the collisional simulation.

V. CONCLUSION

In summary, we present results from one-dimensional particle-in-cell simulations of relativistic laser–solid interactions, concentrating on the sub-cycle dynamics of electron bunches and the emitted attosecond pulses as a function of the laser intensity, plasma density, laser angle of incidence, and spatial and temporal resolution of the simulations. Specifically, we show that for initial conditions of the laser and plasma parameters which yield inefficient attosecond pulses, the time of attosecond pulse emission occurs at $t/T_L \approx 0.5$, at which point the electron bunch has expanded close to the original density of the plasma, resulting in weak attosecond pulse intensities. In contrast, in parameter regimes where the highest attosecond pulse efficiencies are obtained, the attosecond pulses are emitted at a point in time when the electron bunch has its highest peak density, which occurs at times exceeding $0.5T_L$ as a result of the increased displacement of the electron bunch from the initial plasma–vacuum interface.

We find that in collisionless particle-in-cell simulations, there exists a spatial resolution-dependent growth in the peak density of the electron bunch, which does not plateau even at extremely high resolutions. Despite the appearance of these sharp density spikes confined to be within a single cell of the numerical grid, the attosecond pulses and spectra converge with increasing spatial resolution for a given frequency range.

When binary collisions are added to the PIC model, the peak electron bunch density initially exhibits the same growth but eventually converges to a fixed value as the spatial resolution is increased. In general, modeling collisions lower the attosecond pulse intensity except in regimes where $a_0/N_0 \gtrsim 0.6$ at a fixed N_0 and where $N_0 \gtrsim 500$ at a fixed a_0/N_0. The reduction in attosecond pulse intensity for collisional simulations is a consequence of the increased spread in time of the peak Lorentz factors of the emitting electrons, which leads to an earlier frequency cutoff than that obtained in collisionless simulations.

ACKNOWLEDGMENTS

This work was partially supported by the National Science Foundation under Grant Nos. PHY 1806911 and PHY 2206711 and the Department of Energy under Grant No. DE-SC0017907. We gratefully acknowledge the utilization of the EPOCH code for the research output. N.M.F. gratefully acknowledges support from the Program in Plasma Science and Technology (PPST). Support was provided by the LLNL LDRD Program under Project No. 20-ERD-057. Lawrence Livermore National Laboratory is operated by Lawrence Livermore National Security, LLC, for the U.S. Department of Energy, National Nuclear Security Administration under Contract No. DE-AC52-07NA27344.

AUTHOR DECLARATIONS

Conflict of Interest

The authors have no conflicts to disclose.

Author Contributions

Nicholas Maurice Fasano: Conceptualization (equal); Data curation (lead); Formal analysis (lead); Investigation (equal); Visualization (lead); Writing – original draft (lead); Writing – review & editing (equal). **Matthew R. Edwards:** Conceptualization (equal); Writing – original draft (supporting); Writing – review & editing (equal). **Julia Mikhailova:** Conceptualization (equal); Funding acquisition (lead); Writing – original draft (supporting); Writing – review & editing (equal).

DATA AVAILABILITY

The data that support the findings of this study are available from the corresponding author upon reasonable request.

APPENDIX: SPACE AND TIME DISCRETIZATION–NUMERICAL DISPERSION

Relativistic high-harmonic generation experiments are performed in vacuum to avoid the nonlinear effects of high-intensity laser propagation in air. In vacuum, the dispersion relation of electromagnetic waves is independent of wavelength, but the algorithm used in conventional PIC simulations to advance the fields is the FDTD-based Yee scheme, which has a numerical dispersion relation and associated group velocity that can be expressed as follows:[26,27]

$$\omega = \frac{2}{\Delta t}\sin^{-1}(C\sin(k\Delta x/2)), \tag{A1}$$

$$\frac{v_g}{c} = \frac{1}{c}\frac{d\omega}{dk} = \frac{\cos(k\Delta x/2)}{\sqrt{1 - C^2\sin^2(k\Delta x/2)}}. \tag{A2}$$

Inspection of Eq. (A2) shows that, for fixed temporal and spatial resolution, the speed of light in vacuum decreases as the frequency of the radiation increases. In this section, we show that the frequency-dependent group velocity present in the FDTD-based Yee scheme has negligible effect on the propagation of attosecond pulses for significant propagation lengths as a result of needing high spatial resolution to resolve the attosecond pulses at the time of emission. We restrict our focus to one-dimensional particle-in-cell simulations, but the analysis presented here on the frequency-dependent group velocity can be extended to two- or three-dimensional simulations. However, in a two- or three-dimensional geometry, numerical dispersion will result in additional effects such as non-specular reflection of harmonics from the plasma–vacuum interface as has been analyzed previously.[41]

To illustrate the effects of numerical dispersion on the propagation of attosecond pulses, we analyze the reflected electric field using spectrograms. The spectrograms are constructed by first multiplying the reflected electric field by a gating window (here, we use a Gaussian-shaped window with a full width half maximum of $0.5T_L$) with a chosen delay, τ with respect to the center of the reflected laser's temporal envelope. Next, the Fourier transform of the resulting waveform is computed, yielding a spectrum of the gated field. Finally, the full spectrogram is constructed by repeating this process for different delays of the gating window. In Fig. 9, spectrograms of the reflected electric field from four PIC simulations are plotted, where each simulation was performed using a spatial resolution of either $\lambda_L/\Delta x = 1500$ or $\lambda_L/\Delta x = 4000$ and a CFL number of either $C = 0.53$ or $C = 0.95$. For $\lambda_L/\Delta x = 4000$ and $C = 0.95$ [Fig. 9(d)], the spectrogram consists of a vertical line centered at $t = 0$ which indicates that all frequencies were emitted at the same time. As $\lambda_L/\Delta x$ is decreased to 1500 and C is decreased to 0.53, the high-frequency radiation of the spectrogram bends toward later times, reflecting the fact that higher frequencies are traveling slower than the speed of light.

Numerical dispersion causes a temporal chirp in the propagating attosecond pulse as a result of the frequency-dependent propagation speeds. However, we emphasize here that, at the high resolutions needed to resolve the emission of the attosecond pulse at all, the deleterious effects of group velocity mismatch on the attosecond propagation are negligible for significant propagation lengths. Figure 10 illustrates the difference between poorly resolved

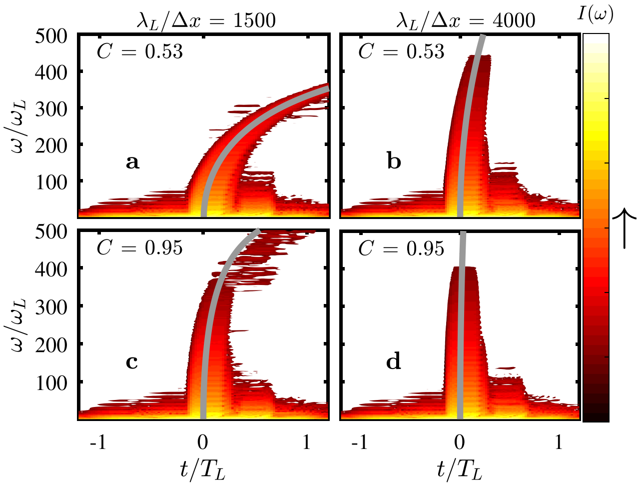

FIG. 9. Spectrograms of the reflected electric field from PIC simulations with (a) $C = 0.53$ and $\lambda_L/\Delta x = 1500$, (b) $C = 0.53$ and $\lambda_L/\Delta x = 4000$, (c) $C = 0.95$ and $\lambda_L/\Delta x = 1500$, and (d) $C = 0.95$ and $\lambda_L/\Delta x = 4000$. The other parameters of the simulations are $\theta = 0°$, $a_0 = 40$, $N_0 = 200$, and particles/cell $= 50$. The reflected electric field propagated for three laser wavelengths before being recorded in time at a fixed spatial location. The gray line is calculated using Eq. (A2) and assumes that all frequencies were emitted at the same time.

attosecond pulses immediately after the time of emission [Fig. 10(a)] and attosecond pulses that have become temporally chirped as a result of numerical dispersion after propagating in vacuum for 28 laser periods [Fig. 10(b)]. For the frequency range used to construct the attosecond pulses in Fig. 10 ($4 < \omega/\omega_L < 10$), a spatial resolution of $\lambda_L/\Delta x \gtrsim = 50$ is needed to accurately resolve the attosecond pulse at the time of emission. After propagating for 28 laser periods, the intensity of the attosecond pulse drops by only a factor of two for $\lambda_L/\Delta x = 50$ and not at all for $\lambda_L/\Delta x \gtrsim 100$.

Since we have an analytic expression for the numerical dispersion of electromagnetic waves in vacuum (gray lines in Fig. 9), we can define a criterion that specifies the smallest wavelength for which the effects of numerical dispersion are negligible based on a given C, Δx, and propagation length. Here, the effects of numerical dispersion are considered significant when radiation at a wavelength, λ_n, has traveled a distance $\lambda_n/2$ less than it would have if it propagated according to the continuous dispersion equation. At this point, the numerically propagated wavelengths greater than or equal to λ_n would have completely destructively interfered with the continuum versions of themselves. According to this criterion, only the cases in Fig. 10(b) with $\lambda_L/\Delta x > 150$ will have suppressed the effects of numerical dispersion.

To get an intuitive feeling for this criterion, we construct analytic spectrograms across a wide range of CFL numbers [Fig. 11(a)] and spatial resolutions [Fig. 11(b)]. As illustrated in Fig. 11(a), the highest resolved frequency approaches the Nyquist–Shannon criterion ($\omega/\omega_L = \lambda_L/2\Delta x$) as the CFL number approaches 1. Theoretically, setting $C = 1$ will allow for dispersion-free propagation, but the simulation will only be marginally stable. Increasing the CFL number from $C = 0.95$ to $C = 0.999$ will suppress numerical dispersion from harmonic order $\omega/\omega_L = 100$ to $\omega/\omega_L = 300$ when $\lambda_L/\Delta x = 1000$ and a propagation distance of $1\lambda_L$ is used. Increasing the spatial resolution will also suppress numerical dispersion [Fig. 11(b)], but the computational expense (memory and time) will increase considerably. For comparison, to suppress numerical dispersion from harmonic order $\omega/\omega_L = 100$ to $\omega/\omega_L = 300$ would require increasing the spatial resolution from $\lambda_L/\Delta x = 1000$ to $\lambda_L/\Delta x = 6000$ when $C = 0.95$ and a propagation distance of $1\lambda_L$ is used. For these reasons, it is desirable to choose C close to one for a particular spatial resolution without resulting in an instability.

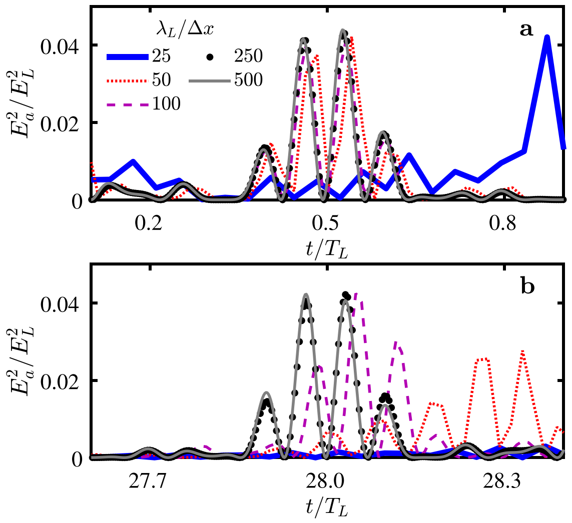

FIG. 10. Effects of spatial resolution on the attosecond pulse temporal profile for the parameters $\theta = 0°$, $a_0 = 40$, $N_0 = 200$, varied $\lambda_L/\Delta x$, particles/cell $= 100$, and $C = 0.95$. (a) Attosecond pulses immediately after emission for five different spatial resolutions. The attosecond pulses are constructed using radiation in the frequency range $4 < \omega/\omega_L < 10$. (b) The same five attosecond pulses but after they have propagated for 28 laser periods.

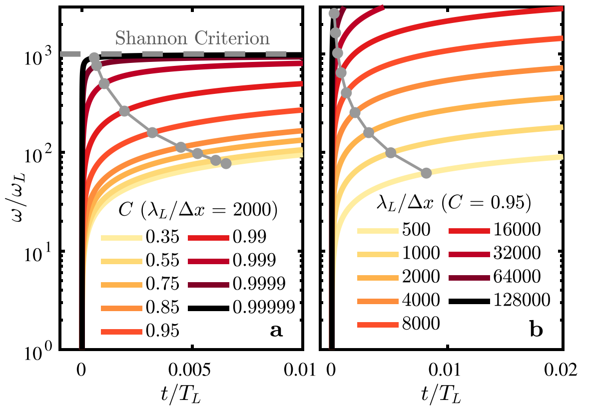

FIG. 11. Analytic spectrograms calculated from Eq. (A2). The calculation assumes all frequencies are emitted at the same time and have propagated for one laser period. (a) Spectrograms for varied spatial resolution and $C = 0.95$. (b) Spectrograms for varied CFL number and $\lambda_L/\Delta x = 2000$. The gray dots are located at a frequency (ω_n) such that $t/T_L = \omega_L/(2\omega_n)$.

We performed a set of simulations with varying spatial and temporal resolution with C in the range of 0.95–0.999 999 and $\lambda_L/\Delta x$ in the range of 100–50 000 (Fig. 12). Figure 12(a) shows the reflected field's spectrum for three different spatial resolutions and $C = 0.999\,999$. For simulations with $\lambda_L/\Delta x < 10\,000$, an instability develops which has the fastest growth rate at the Nyquist frequency. To achieve convergence in spectral intensity at $\omega/\omega_L = 100$ requires using a spatial resolution of $\lambda_L/\Delta x > 10\,000$, which is an order of magnitude higher than if a lower CFL number of $C = 0.95$ was used. For comparison, the spectrum obtained from a simulation with $C = 0.95$ and $\lambda_L/\Delta x = 1000$ is plotted in black in Fig. 12(a).

In Fig. 12(b), the spectral efficiency is plotted as a function of $\lambda_L/\Delta x$ for three different harmonic orders ($\omega_n/\omega_L = 3$, 25, 200) and four different CFL numbers. For C values between 0.95 and 0.99, the numerical error resulting from the instability is negligible for all $\lambda_L/\Delta x$. However, for $C > 0.99$, the instability affects the spectral energy for both low ($\omega_n/\omega_L = 3$) and high ($\omega_n/\omega_L = 200$) harmonic orders and requires at least an order of magnitude higher spatial resolution for the spectral efficiency to converge to a fixed value. These results suggest there is no advantage to using a CFL number greater than 0.99 to mitigate numerical dispersion since a higher CFL number requires increased spatial resolution to suppress the induced numerical instabilities.

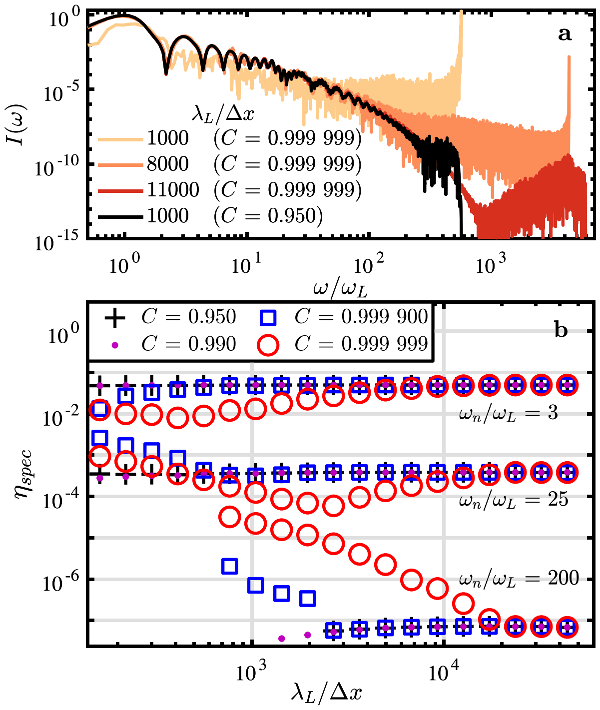

FIG. 12. Numerical error in PIC simulations as a result of choosing a CFL number close to the stability limit ($C = 1$) for the parameters $\theta = 0°$, $a_0 = 40$, $N_0 = 200$, particles/cell = 50, varied $\lambda_L/\Delta x$, and varied C. (a) Spectral intensity of the total reflected field for $C = 0.999\,999$ and $\lambda_L/\Delta x = 1000$, 8000, and 11 000 as well as for $C = 0.95$ and $\lambda_L/\Delta x = 1000$. (b) Spectral efficiency contained in the frequency range $-0.5 + \omega_n/\omega_L < \omega/\omega_L < 0.5 + \omega_n/\omega_L$ for the nth harmonic order as a function of $\lambda_L/\Delta x$ for four different CFL numbers.

In summary, in this appendix, we showed that the minimum spatial resolution needed to resolve attosecond pulse emission is also sufficient to suppress the effects of numerical dispersion on the attosecond pulse temporal profiles for significant propagation lengths. In addition, although choosing CFL numbers close to one is a promising way to achieve dispersion-free propagation of harmonics, it leads to numerical errors as it is close to the stability limit. These numerical errors can be corrected only by increasing the spatial resolution, which requires more computational expense and largely offsets the advantages for choosing a higher CFL number.

REFERENCES

[1] D. von der Linde and K. Rzazewski, Appl. Phys. B **63**, 499 (1996).
[2] P. Gibbon, Phys. Rev. Lett. **76**, 50 (1996).
[3] R. Lichters, J. Meyer-ter-Vehn, and A. Pukhov, Phys. Plasmas **3**, 3425 (1996).
[4] P. Norreys, M. Zepf, S. Moustaizis, A. Fews, J. Zhang, P. Lee, M. Bakarezos, C. Danson, A. Dyson, P. Gibbon *et al.*, Phys. Rev. Lett. **76**, 1832 (1996).
[5] S. Gordienko, A. Pukhov, O. Shorokhov, and T. Baeva, Phys. Rev. Lett. **93**, 115002 (2004).
[6] B. Dromey, M. Zepf, A. Gopal, K. Lancaster, M. Wei, K. Krushelnick, M. Tatarakis, N. Vakakis, S. Moustaizis, R. Kodama *et al.*, Nat. Phys. **2**, 456 (2006).
[7] C. Thaury and F. Quéré, J. Phys. B: At. Mol. Opt. Phys. **43**, 213001 (2010).
[8] P. Heissler, P. Tzallas, J. M. Mikhailova, K. Khrennikov, L. Waldecker, F. Krausz, S. Karsch, D. Charalambidis, and G. D. Tsakiris, New J. Phys. **14**, 043025 (2012).
[9] C. Rödel, D. an der Brügge, J. Bierbach, M. Yeung, T. Hahn, B. Dromey, S. Herzer, S. Fuchs, A. G. Pour, E. Eckner *et al.*, Phys. Rev. Lett. **109**, 125002 (2012).
[10] F. Dollar, P. Cummings, V. Chvykov, L. Willingale, M. Vargas, V. Yanovsky, C. Zulick, A. Maksimchuk, A. Thomas, and K. Krushelnick, Phys. Rev. Lett. **110**, 175002 (2013).
[11] P. Heissler, A. Barna, J. M. Mikhailova, G. Ma, K. Khrennikov, S. Karsch, L. Veisz, I. Földes, and G. D. Tsakiris, Appl. Phys. B **118**, 195 (2015).
[12] D. an der Brügge and A. Pukhov, Phys. Plasmas **17**, 033110 (2010).
[13] B. Dromey, S. Rykovanov, M. Yeung, R. Hörlein, D. Jung, D. C. Gautier, T. Dzelzainis, D. Kiefer, S. Palaniyppan, R. Shah, J. Schreiber, H. Ruhl, J. C. Fernandez, C. L. S. Lewis, M. Zepf, and B. M. Hegelich, Nat. Phys. **8**, 804 (2012).
[14] J. M. Mikhailova, M. V. Fedorov, N. Karpowicz, P. Gibbon, V. T. Platonenko, A. M. Zheltikov, and F. Krausz, Phys. Rev. Lett. **109**, 245005 (2012).
[15] M. Cherednychek and A. Pukhov, Phys. Plasmas **23**, 103301 (2016).
[16] M. R. Edwards and J. M. Mikhailova, Sci. Rep. **10**, 5154 (2020).
[17] S. Cousens, B. Reville, B. Dromey, and M. Zepf, Phys. Rev. Lett. **116**, 083901 (2016).
[18] A. Gonoskov, Phys. Plasmas **25**, 013108 (2018).
[19] M. R. Edwards, N. M. Fasano, and J. M. Mikhailova, Phys. Rev. Lett. **124**, 185004 (2020).
[20] M. R. Edwards, V. T. Platonenko, and J. M. Mikhailova, Opt. Lett. **39**, 6823 (2014).
[21] P. Zhang and A. G. R. Thomas, Appl. Phys. Lett. **106**, 131102 (2015).
[22] M. R. Edwards and J. M. Mikhailova, Phys. Rev. A **93**, 023836 (2016).
[23] M. R. Edwards and J. M. Mikhailova, Phys. Rev. Lett. **117**, 125001 (2016).
[24] M. Yeung, S. Rykovanov, J. Bierbach, L. Li, E. Eckner, S. Kuschel, A. Woldegeorgis, C. Rödel, A. Sävert, G. G. Paulus, M. Coughlan, B. Dromey, and M. Zepf, Nat. Photonics **11**, 32 (2017).
[25] R. W. Hockney and J. W. Eastwood, *Computer Simulation Using Particles* (CRC Press, 2021).
[26] A. Pukhov, J. Plasma Phys. **61**, 425 (1999).
[27] C. K. Birdsall and A. B. Langdon, *Plasma Physics via Computer Simulation* (CRC Press, 2018).
[28] T. D. Arber, K. Bennett, C. S. Brady, A. Lawrence-Douglas, M. G. Ramsay, N. J. Sircombe, P. Gillies, R. G. Evans, H. Schmitz, A. R. Bell, and C. P. Ridgers, Plasma Phys. Controlled Fusion **57**, 113001 (2015).

[29] K. Yee, IEEE Trans. Antennas Propag. **14**, 302 (1966).

[30] A. Pukhov, J. Comput. Phys. **418**, 109622 (2020).

[31] A. Blinne, D. Schinkel, S. Kuschel, N. Elkina, S. G. Rykovanov, and M. Zepf, Comput. Phys. Commun. **224**, 273 (2018).

[32] F. Li, P. Yu, X. Xu, F. Fiuza, V. K. Decyk, T. Dalichaouch, A. Davidson, A. Tableman, W. An, F. S. Tsung, R. A. Fonseca, W. Lu, and W. B. Mori, Comput. Phys. Commun. **214**, 6 (2017).

[33] B. B. Godfrey and J.-L. Vay, J. Comput. Phys. **267**, 1 (2014).

[34] X. Xu, P. Yu, S. F. Martins, F. S. Tsung, V. K. Decyk, J. Vieira, R. A. Fonseca, W. Lu, L. O. Silva, and W. B. Mori, Comput. Phys. Commun. **184**, 2503 (2013).

[35] B. M. Cowan, D. L. Bruhwiler, J. R. Cary, E. Cormier-Michel, and C. G. R. Geddes, Phys. Rev. Spec. Top. -Accel. Beams **16**, 041303 (2013).

[36] R. Lehe, A. Lifschitz, C. Thaury, V. Malka, and X. Davoine, Phys. Rev. Spec. Top. -Accel. Beams **16**, 021301 (2013).

[37] J. B. Cole, IEEE Trans. Antennas Propag. **50**, 1185 (2002).

[38] B. B. Godfrey, J. Comput. Phys. **15**, 504 (1974).

[39] J.-L. Vay, I. Haber, and B. B. Godfrey, J. Comput. Phys. **243**, 260 (2013).

[40] H. Vincenti and J. L. Vay, Comput. Phys. Commun. **200**, 147 (2016).

[41] G. Blaclard, H. Vincenti, R. Lehe, and J. L. Vay, Phys. Rev. E **96**, 033305 (2017).

[42] H. Vincenti and J.-L. Vay, Comput. Phys. Commun. **228**, 22 (2018).

[43] H. Kallala, J.-L. Vay, and H. Vincenti, Comput. Phys. Commun. **244**, 25 (2019).

[44] H. Vincenti, Phys. Rev. Lett. **123**, 105001 (2019).

[45] J. M. Dawson, Rev. Mod. Phys. **55**, 403 (1983).

[46] T. Takizuka and H. Abe, J. Comput. Phys. **25**, 205 (1977).

[47] K. Nanbu, Phys. Rev. E **55**, 4642 (1997).

[48] K. Nanbu and S. Yonemura, J. Comput. Phys. **145**, 639 (1998).

[49] Y. Sentoku and A. J. Kemp, J. Comput. Phys. **227**, 6846 (2008).

[50] F. Pérez, L. Gremillet, A. Decoster, M. Drouin, and E. Lefebvre, Phys. Plasmas **19**, 083104 (2012).

[51] D. P. Higginson, I. Holod, and A. Link, J. Comput. Phys. **413**, 109450 (2020).

[52] E. P. Alves, W. B. Mori, and F. Fiuza, Phys. Rev. E **103**, 013306 (2021).

[53] Y. M. Mikhailova, V. T. Platonenko, and A. B. Savel'ev, Quantum Electron. **35**, 38 (2005).

[54] Y. Zhao, R. Lehe, A. Myers, M. Thévenet, A. Huebl, C. B. Schroeder, and J.-L. Vay, Phys. Plasmas **27**, 113105 (2020).

[55] S. Weber, G. Bonnaud, and J.-C. Gauthier, Phys. Plasmas **8**, 387 (2001).

[56] F. Peano, M. Marti, L. O. Silva, and G. Coppa, Phys. Rev. E **79**, 025701 (2009).

[57] A. Bourdier, Phys. Fluids **26**, 1804 (1983).

[58] P. Gibbon, A. Andreev, E. Lefebvre, G. Bonnaud, H. Ruhl, J. Delettrez, and A. R. Bell, Phys. Plasmas **6**, 947 (1999).

[59] S. Gordienko and A. Pukhov, Phys. Plasmas **12**, 043109 (2005).